Bulletin of the Seismological Society of America, Vol. 94, No. 1, pp. 155–170, February 2004

Effects of Fault Dip and Slip Rake Angles on Near-Source Ground Motions: Why Rupture Directivity Was Minimal in the 1999 Chi-Chi, Taiwan, Earthquake

by Brad T. Aagaard,* John F. Hall, and Thomas H. Heaton

Abstract We study how the fault dip and slip rake angles affect near-source ground velocities and displacements as faulting transitions from strike-slip motion on a vertical fault to thrust motion on a shallow-dipping fault. Ground motions are computed for five fault geometries with different combinations of fault dip and rake angles and common values for the fault area and the average slip. The nature of the shear-wave directivity is the key factor in determining the size and distribution of the peak velocities and displacements. Strong shear-wave directivity requires that (1) the observer is located in the direction of rupture propagation and (2) the rupture propagates parallel to the direction of the fault slip vector. We show that predominantly along-strike rupture of a thrust fault (geometry similar in the Chi-Chi earthquake) minimizes the area subjected to large-amplitude velocity pulses associated with rupture directivity, because the rupture propagates perpendicular to the slip vector; that is, the rupture propagates in the direction of a node in the shear-wave radiation pattern. In our simulations with a shallow hypocenter, the maximum peak-to-peak horizontal velocities exceed 1.5 m/sec over an area of only 200 km^2 for the 30°-dipping fault (geometry similar to the Chi-Chi earthquake), whereas for the 60°- and 75°-dipping faults this velocity is exceeded over an area of 2700 km^2. These simulations indicate that the area subjected to large-amplitude long-period ground motions would be larger for events of the same size as Chi-Chi that have different styles of faulting or a deeper hypocenter.

Introduction

In the past decade, several earthquakes near large urban areas have caused considerable damage, including the 1994 Northridge, California, the 1995 Hyogo-Ken Nanbu (Kobe), Japan, the 1999 Izmit and Duzce, Turkey, and the 1999 Chi-Chi, Taiwan, earthquakes. These earthquakes and their associated ground-motion records increased the awareness of the destructive capability and characteristics of near-source ground motions (e.g., see Olsen and Archuleta, 1996; Somerville *et al.*, 1997; Hisada *et al.*, 1998; Kamae and Irikura, 1998; Pitarka *et al.*, 1998; Huang *et al.*, 2000; Oglesby *et al.*, 2000; Ouchi *et al.*, 2001; Chen *et al.*, 2001). Two factors control the amplitude of near-source ground motions: rupture directivity and proximity to the fault. At all locations in the near field, the directivity of the rupture affects the amplitude of the motion. Additionally, at locations very close to the fault trace, the static offset also directly contributes to the amplitude of the motion. This means that for events of the same size, which have similar static offsets, changes in the rupture directivity largely determine the variations in the amplitude of the near-source ground motions from one event to another. The primary factor controlling the size of the directivity effect is not simply the distance the rupture propagates toward a location, but the distance the rupture propagates toward a location while it is parallel to the direction of slip. Consequently, the dimensions and the dip angle of the fault, the direction of slip (slip rake angle), and the location of the hypocenter all play critical roles in determining the character and amplitude of near-source ground motions.

Early efforts aimed at understanding near-source ground motions focused on simple numerical models (e.g., Haskell, 1969; Archuleta and Frazier, 1978; Archuleta and Hartzell, 1981). More recently, some researchers have focused on specific ground-motion recordings (Iwan and Chen, 1994) or damage near a surface rupture (Allen *et al.*, 1998) to infer the characteristics of near-source ground motions. Three-dimensional simulations have been used to understand the physics of near-source ground motions for specific events

*Present address: USGS, MS977, 345 Middlefield Rd., Menlo Park, California 94025.

(e.g., Olsen *et al.*, 1997; Nielsen and Olsen, 2000; Oglesby and Day, 2001). Researchers have also used them to examine hypothetical scenarios. Olsen *et al.* (1995) and Graves (1998) examined near-source ground motions for ruptures on the San Andreas fault, and Olsen and Archuleta (1996) considered various scenarios within the Los Angeles area. Whereas these previous studies help to explain patterns of damage in particular earthquakes or what such patterns might be for some future event, they generally do not shed light on the fundamental characteristics of near-source ground motions and how these vary with changes in the seismic source parameters. Dynamic rupture models have improved our understanding of how near-source ground motions develop from the basic features of the rupture process (Olsen *et al.*, 1997; Inoue and Miyatake, 1998; Oglesby *et al.*, 2000; Aagaard *et al.*, 2001b), but only a couple of these studies (Oglesby *et al.*, 2000; Aagaard *et al.*, 2001b) have systematically explored how the source parameters affect the near-source ground motions.

We complement these two efforts and other work (Aagaard *et al.*, 2001a) that used kinematic source models to systematically examine source parameters and near-source ground motions by focusing on an event of a specific size and determining how changes in the style of faulting, in particular the fault dip and slip rake angles, affect the near-source ground motions. We examine the distribution of shaking and the characteristics of the near-source ground motions, as well as how these change in response to variations in the fault dip and slip rake angles for two hypocenters. We consider several measures of the ground motions, including the area where the ground motion exceeds a given level and the mean maximum amplitude of the motion as a function of distance from the fault. Furthermore, by selecting a parameter space that includes a scenario that approximately matches the 1999 Chi-Chi earthquake in Taiwan, we explore the role that the style of faulting played in determining the area subjected to high-intensity long-period (2 sec and longer) shaking in the Chi-Chi earthquake.

These long-period ground motions place the greatest demand on structures with similar elastic periods, such as tall buildings. However, velocity pulses with amplitudes of about 1 m/sec are large enough to cause yielding in structures with significantly shorter periods (Hall, 1995, 1997). Once a structure begins to yield, the displacement amplitude becomes very important, with larger displacements resulting in greater yielding and damage. For example, using simulations of steel-frame buildings, Hall, (1997) found that the motion recorded at the Lucerne Valley station in the 1992 Landers earthquake with a velocity pulse duration of about 4 sec could, in addition to causing collapse of a 20-story building (3.5-sec fundamental elastic period), also generate considerable yielding in a 6-story structure (1.5-sec fundamental elastic period).

Observations from the Northridge earthquake support these findings. Boatwright *et al.* (2001) noted that the distribution of red-tagged buildings (mostly low-rise structures with periods shorter than 1 sec) following the 1994 Northridge earthquake closely resembled the distribution of peak ground velocity for periods of around 1.5 sec. Likewise, Wald *et al.* (1999) developed a linear regression between peak velocity and modified Mercalli intensity for eight California earthquakes. This implies that velocity, not acceleration, correlates well with damage across the general population of structures. Thus, although the bandwidth of the simulations in our study is restricted to periods of 2 sec and longer and is most applicable to structures with similar fundamental elastic periods, the amplitudes of these long-period ground motions also play a role in the response of structures with shorter periods.

Earthquake Scenarios

We compute the near-source ground motions for two hypocenters for each of five different pairs of fault dip and slip rake angles. We also select a realistic fault length-to-width ratio for each dip angle. The scenarios vary from a pure strike-slip rupture on a long, narrow fault to a pure thrust rupture on a significantly shorter and wider fault.

Methodology

We follow the general methodology of our previous work involving simulations of near-source ground motions, so this section contains only a brief summary of the methods used in the earthquake simulations. Aagaard (1999) and Aagaard *et al.* (2001a) provided detailed discussions of the methodology. As discussed later, this study improves upon our previous characterizations of the seismic source; in particular, the length scales of the spatial heterogeneity in the final slip are compatible with those found in kinematic source inversions, and we allow the rupture speed to vary as a function of the direction of propagation relative to the direction of slip.

We discretize the three-dimensional domain using linear tetrahedral finite elements. This transforms the three-dimensional dynamic elasticity equation,

$$\lambda u_{k,kj}\delta_{ij} + \mu(u_{i,jj} + u_{j,ij}) = \rho\ddot{u}_i, \qquad (1)$$

into a matrix differential equation,

$$[M]\{\ddot{u}(t)\} + [C]\{\dot{u}(t)\} + [K]\{u(t)\} = \{F(t)\}, \qquad (2)$$

where $[M]$ denotes the mass matrix, $[C]$ denotes the damping matrix, $[K]$ denotes the stiffness matrix, $\{F(t)\}$ denotes the force vector at time t, and $\{u(t)\}$ denotes the displacement vector at time t. Our discretization of the finite-element model limits the simulation to wave propagation for waves with periods of 2.0 sec and longer.

Anelastic attenuation is not included because it has little effect on long-period near-source ground motions, so the only contribution to the damping matrix comes from the absorbing boundaries on the lateral sides and bottom of

the domain. These absorbing boundaries prevent waves from reflecting off the truncated sides of the domain and contaminating the solution.

We model the earthquake by creating dislocations in the finite-element model that mimic the slip on a fault. In the scenarios discussed here, we specify the slip time history at each point on the fault, where the time history follows the integral of Brune's far-field time function with the final slip and peak slip rate as parameters.

Simulation Domain

In each of the scenarios, the domain is 160 km long, 80 km wide, and 40 km deep, as shown in Figure 1. The material properties vary only as a function of depth, as illustrated in Figure 2. This set of material properties represents the average variations in Taiwan and corresponds to the variation in a region without a deep sedimentary basin (Ma *et al.*, 1996, 2001).

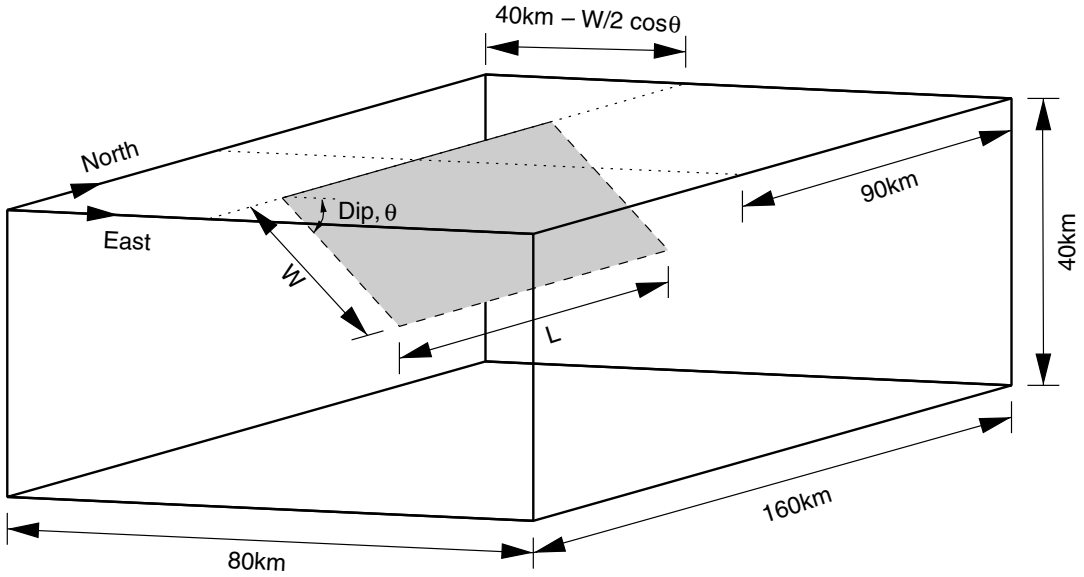

Figure 1. Geometry of the simulation domain. The fault has a dip angle of θ, a length of L, and a width of W. The center of the fault lies 10 km south of the center of the domain. The dotted line running east–west sits above the center of the fault, whereas the dotted line running north–south intersects the fault trace.

Earthquake Source Parameters

Table 1 gives the five pairs of fault dip and slip rake angles along with the fault lengths and widths for the different fault geometries. For the five fault geometries, we chose fault dip angles uniformly distributed between 90° and 30° with rake angles uniformly distributed between 0° and 90°. Similarly, the lengths of the faults decrease linearly from 120 to 80 km long while maintaining an area of 2400 km^2. The 80-km-long and 30-km-wide fault, which has a dip angle of 30°, roughly matches the geometry of the 1999 Chi-Chi earthquake in Taiwan. Inversions for the source characteristics indicate this earthquake had a rupture length of between 80 and 100 km, a rupture width of between 30 and 40 km, and a dip angle of 20°–30° (Huang *et al.*, 2000; Ma *et al.*, 2000; Johnson *et al.*, 2001; Ji *et al.*, 2001). By varying the length-to-width ratios as we change the slip rake angle, we create realistic fault geometry for each of the five fault dip angles.

Based on the regression relations of Wells and Coppersmith (1994) between fault geometry and average slip coupled with these fault dimensions, we chose a common average slip of 2.9 m for the scenarios. This average slip is smaller than the average slip estimated for the Chi-Chi earthquake, so our fault with a dip angle of 30° and our choice of material properties has a moment magnitude of only 7.4

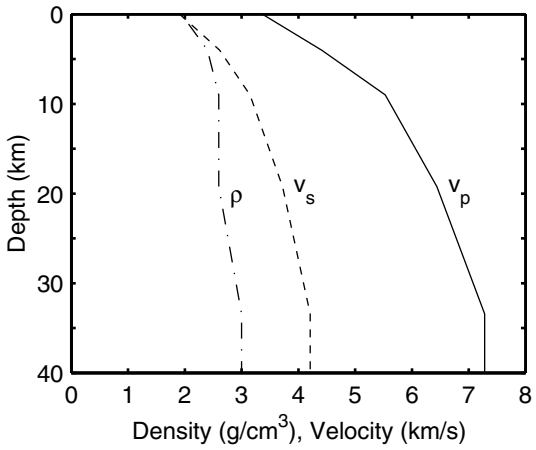

Figure 2. Dilatational wave speed (v_p), shear wave speed (v_s), and mass density (ρ) as a function of depth.

compared with the moment magnitude of 7.6–7.7 estimated for the Chi-Chi earthquake. For each fault the slip rake angles are uniform and remain constant during the rupture. We also use a uniform peak slip rate of 2.0 m/sec in the slip time history, which, for final slips of around 3 m, gives slip durations compatible with those found in kinematic source inversions (Heaton, 1990; Somerville *et al.*, 1997).

We create the distributions of slip by low-pass filtering random distributions. Starting with a uniform random distribution on a 1.0-km uniform grid (which is coarser than the node spacing in the finite-element model), we low-pass filter along the fault strike and then along the dip using a first-order Butterworth filter. We also taper the slip along the buried edges of the fault. Whereas the distributions for each fault geometry all have an average slip of 2.9 m, the maximum slip ranges from 5.7 to 7.1 m because we start with different random distributions for each fault geometry. Figure 3 shows the distribution of final slip for the fault with a dip angle of 60°. The slip distributions for the other fault geometries are similar. Although a power-law spectral falloff would create slip distributions that better match what is found in kinematic source inversions (Somerville *et al.*, 1997; Mai and Beroza, 2002), the long-period near-source ground motions are relatively insensitive to the distribution of slip compared with the hypocenter location and the rupture speed (Aagaard *et al.*, 2001b), so that the dominant features of the ground motions do not change when using a low-pass filtered random distribution compared with a power-law filtered random distribution.

Figure 4 shows the two hypocenters we consider for each dip angle of the fault. The shallow hypocenter sits middepth at the southern quarter point of the fault and corresponds to a highly unilateral rupture, whereas the deep hypocenter sits 5.0 km up-dip from the bottom center of the fault and corresponds to a bilateral case with more up-dip rupture. For strike-slip faulting the ruptures propagate mostly in the mode-II direction (parallel to slip and a local maximum in shear-wave radiation pattern) for both hypocenters. On the other end of the spectrum, for pure thrust faulting and the shallow hypocenter the rupture propagates primarily in the mode-III direction (perpendicular to slip and a node in the shear-wave radiation pattern) with very little propagation in the mode-II direction; for pure thrust faulting and the deep hypocenter, the amount of rupture in the mode-II direction increases significantly.

The rupture speed determines when slip begins at each point on the fault. Numerous dynamic rupture simulations (e.g., Andrews, 1976; Day, 1982; Madariaga *et al.*, 1998; Aagaard *et al.*, 2001b) indicate that ruptures propagate slightly slower in the direction perpendicular to slip (mode-III direction) compared with the direction parallel to slip (mode-II direction). Therefore, instead of an isotropic rupture speed, we independently specify the rupture speed to be 85% of the local shear-wave speed in the mode-II direction (parallel to the slip direction) and 20% slower in the mode-III direction (perpendicular to the slip direction), as illustrated in Figure 4.

Table 1
Seismic Source Parameters for Each Pair of Fault Dip and Slip Rake Angles

Dip Angle (deg)	Rake Angle (deg)	Fault Length (km)	Fault Width (km)	Average Slip (m)	Peak Slip Rate (m/sec)	Rupture Speed (%v_s)
90	0.0	120	20			
75	22.5	110	22			
60	45.0	100	24	2.9	2.0	85% parallel to slip
45	67.5	90	27			68% perpendicular to slip
30	90.0	80	30			

The style of faulting smoothly transitions from pure strike-slip motion on a long, narrow fault to pure thrust motion on a much shorter, wider fault. The rupture speed is set relative to the local shear-wave speed, v_s.

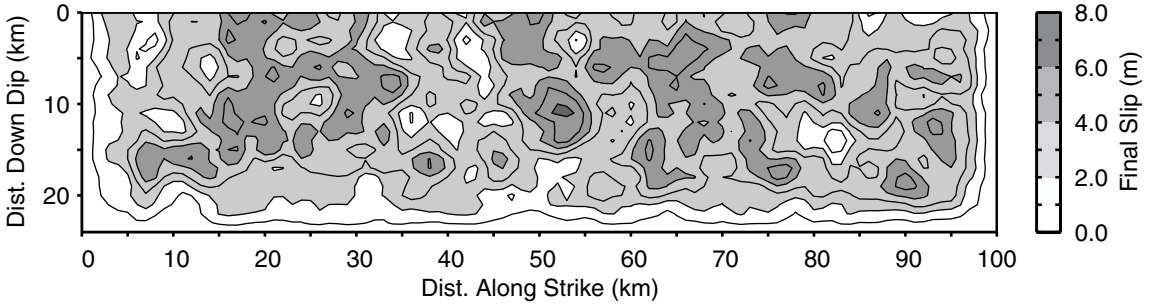

Figure 3. Distribution of final slip for the fault that has a dip angle of 60°. The distribution is a low-pass filtered random distribution. The distributions for the other geometries are similar.

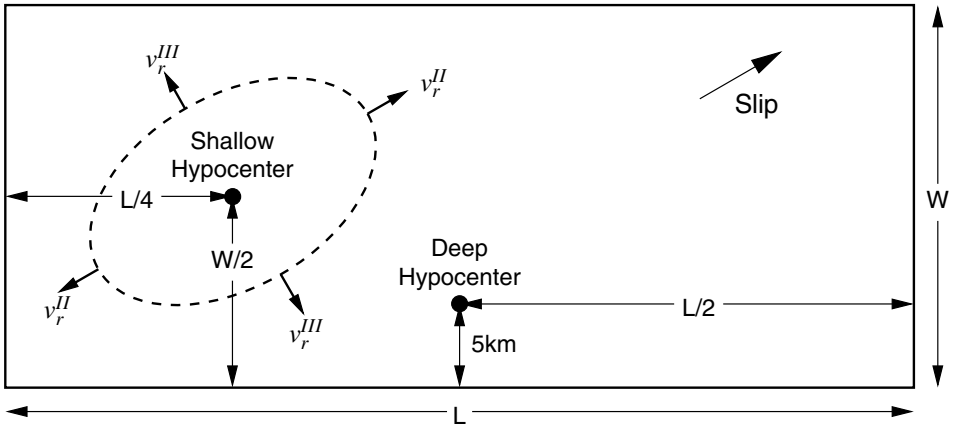

Figure 4. Relative locations of the shallow and deep hypocenters on the fault surface, which has a length of *L* and a width of *W*. The shallow hypocenter lies middepth at a quarter point, and the deep hypocenter lies midway along strike 5 km up-dip from the bottom of the fault. The shallow hypocenter corresponds to the general location of the hypocenter in the Chi-Chi earthquake. The dashed ellipse identifies the rupture front at some point in time propagating away from the shallow hypocenter and illustrates how the rupture speed is set independently in the mode-II (v_r^{II}) and mode-III (v_r^{III}) directions.

Scenario Nomenclature

The name of each scenario corresponds to the dip angle of the fault, the slip rake angle, and the location of the hypocenter. For example, Dip90Rk0HySh refers to the scenario where the fault has a dip angle of 90° and a slip rake angle of 0° and the rupture begins at the shallow hypocenter. Similarly, Dip45Rk68HyDp refers to the scenario where the fault has a dip angle of 45° and a slip rake angle of 67.5° and the rupture begins at the deep hypocenter.

Results

Overview of Rupture Behavior and Ground Motions

We begin by examining how the general characteristics of the rupture behavior and resulting ground motions change with the fault dip and slip rake angles. Additional results and figures can be found in Aagaard *et al.* (2002). In scenario Dip90Rk0HySh, the rupture propagates fastest along the strike of the fault. As we vary the style of faulting across the scenarios by decreasing the dip angle of the fault and increasing the rake angle of slip so that it has a larger vertical component, the rupture speed along the strike decreases while the rupture speed up-dip increases. For the case of the fault at a dip angle of 45° and a rake angle of 67.5°, the fastest rupture speed occurs 22.5° off the up-dip and down-dip directions. This creates asymmetry in the propagation of the rupture for the centrally located deep hypocenter.

Due to the existence of surface rupture in the layered medium, surface waves in the form of combinations of Love and Rayleigh waves dominate the long-period ground motions. As the rupture propagates in scenario Dip90Rk0HySh, large-amplitude Love waves with amplitudes approaching 2.0 m/sec form in the region where the propagation direction generally coincides with the slip direction, which in this case is north of the epicenter. The particle motion for these waves is in the east–west direction (perpendicular to the fault trace). The Love-wave amplitudes generally build along the length of the fault as the rupture reinforces the waves and then begin steadily decreasing upon reaching the northern tip of the fault. The heterogeneous distribution of slip disrupts the reinforcement of the Love waves, so that the amplitudes undergo minor fluctuations as they grow.

As the dip angle of the fault decreases and the vertical component of slip increases, the rupture generates Love waves less effectively and becomes more effective at generating Rayleigh waves. The rotation of the slip direction toward the dip direction results in reinforcement of the *SV* waves (shear waves with particle motion in the vertical direction) emanating from an angle of 45° with respect to the slip direction. These *SV* waves produce Rayleigh waves as they hit the ground surface. Consequently, the largest Rayleigh waves (with amplitudes near 1.5 m/sec) occur northwest of the epicenter; the particle motions are retrograde with the largest horizontal component in the northwest–southeast direction.

Maximum Displacements and Velocities

Choices for measuring the intensity of the shaking include the maximum amplitude of the motion and the maximum peak-to-peak amplitude of the motion, where we measure the peak-to-peak amplitude using consecutive peaks. In practice, the greatest difference between the two occurs for the case of double-sided, symmetric displacement or velocity pulses, as shown in Figure 5. A displacement ramp and the corresponding single-sided velocity pulse roughly approximate the ground motion at a location with a static off-

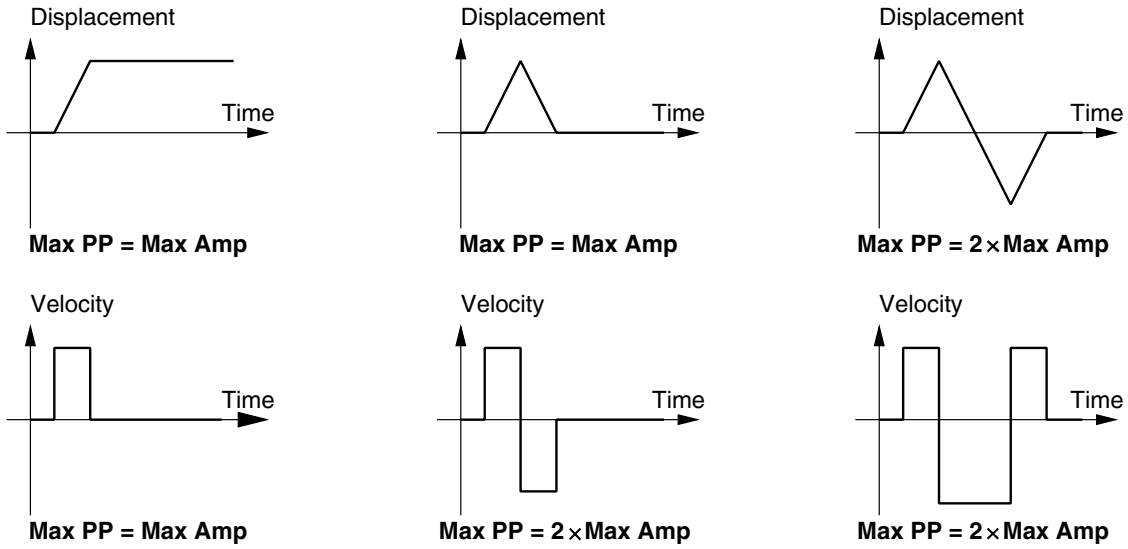

Figure 5. Illustration of how the peak-to-peak displacement and velocity amplitudes compare to the maximum amplitudes for three different types of ground motions: a displacement ramp and corresponding single-sided velocity pulse (left), a single-sided displacement pulse and corresponding double-sided velocity pulse (center), and a double-sided displacement pulse and corresponding velocity pulses (right). Except for the case of double-sided displacements, which are generally associated with surface waves, the maximum peak-to-peak displacements (measured using consecutive peaks) match the maximum displacements. On the other hand, the maximum peak-to-peak velocities exceed the maximum velocities, except for the case in which there is a large static offset.

set. In this case, there is no difference between the maximum peak-to-peak amplitude and the maximum amplitude. A single-sided displacement pulse and the corresponding double-sided velocity pulse roughly approximate the ground motion at a location without a static offset and no surface waves. Whereas the maximum displacement equals the maximum peak-to-peak displacement, the maximum peak-to-peak velocity exceeds the maximum velocity by up to a factor of 2. Finally, a double-sided displacement pulse and the corresponding velocity pulses roughly approximate the ground motion at a location with large-amplitude surface waves and no static offset. In this case, the maximum peak-to-peak displacement and velocity amplitudes can both be up to twice the maximum amplitudes. We will use the maximum magnitude of the displacement and the maximum peak-to-peak velocity as measures of ground-motion intensity because double-sided velocity pulses place a greater demand on structures than single-sided velocity pulses (Hall *et al.*, 1995).

In scenario Dip90Rk0HySh, the maximum horizontal displacements and maximum peak-to-peak horizontal velocities increase along the strike of the fault north and south of the epicenter as shown in Figure 6. This effect is much more pronounced north of the epicenter because the rupture extends much further in this direction compared with south of the epicenter. The amplitudes also decay rapidly with distance away from the surface trace of the fault. The maximum horizontal displacement is 2.6 m, and the maximum peak-to-peak horizontal velocity is 2.6 m/sec.

As the dip of the fault decreases and the vertical component of slip increases, the pattern of shaking becomes much more asymmetric with two clear features: (1) the maximum horizontal displacements on the hanging wall (above the fault) increase and follow the variations in the distribution of slip, and (2) the strongest shaking remains concentrated in the region with the maximum directivity. These trends are visible in Figure 7, which displays the maximum displacements and maximum peak-to-peak velocities for scenario Dip60Rk45HySh. The steep dip of the fault and the rake angle of 45° lead to large Love and Rayleigh waves that propagate toward the northwest. As a result, a large region emanating off to the northwest from the northern end of the fault experiences maximum displacements exceeding 1.0 m and maximum peak-to-peak velocities exceeding 2.0 m/sec.

With the shallow hypocenter, as we transition from strike-slip motion to thrust motion, the rupture continues to propagate mostly along the strike of the fault so that the rupture direction becomes less aligned with the slip direction. In other words, the rupture switches from propagating in the mode-II direction, which is a local maximum in the shear-wave radiation pattern, to propagating in the mode-III direction, which is a node in the shear-wave radiation pattern. In our limiting case where the fault dip angle is 30° with pure thrust faulting, the inability of the rupture to effectively reinforce Love or Rayleigh waves leads to much smaller velocities at most locations on the ground surface (Fig. 8). Although the maximum velocities do reach 1.4 m/

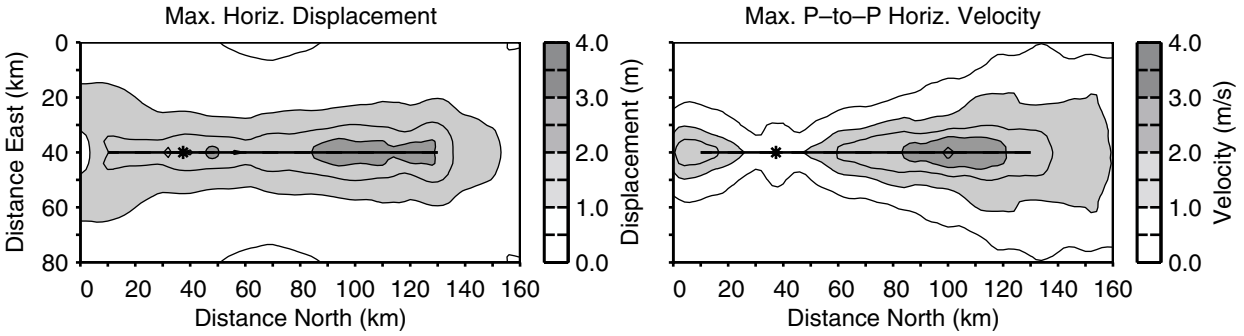

Figure 6. Maximum amplitude of the horizontal displacements and maximum peak-to-peak horizontal velocities on the ground surface for scenario Dip90Rk0HySh. The thick solid line shows the surface trace of the fault, and the asterisk identifies the epicenter. The maximum displacements and velocities generally increase along the fault away from the epicenter and then decrease steadily past the ends of the fault.

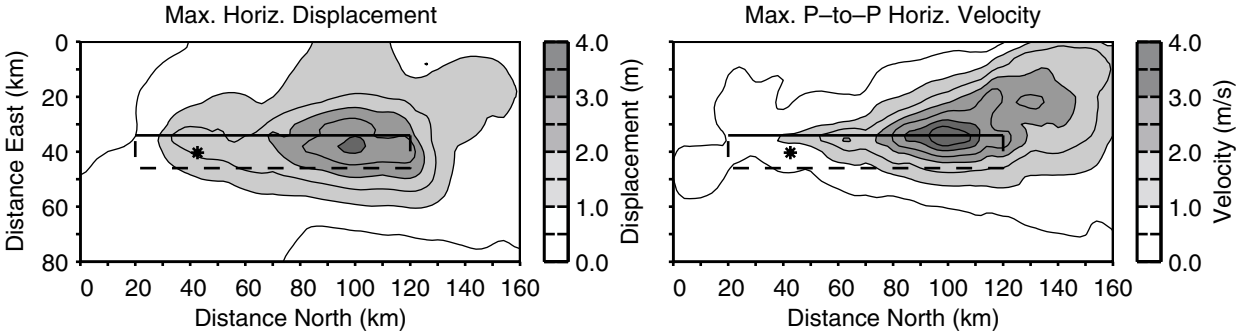

Figure 7. Maximum horizontal displacements and maximum peak-to-peak horizontal velocities on the ground surface for scenario Dip60Rk45HySh. The thick solid line shows the surface trace of the fault, the thick dashed line indicates the surface projection of the buried edges of the fault, and the asterisk identifies the epicenter. The maximum displacements and velocities generally increase along the fault away from the epicenter with a large region of intense shaking extending to the northwest.

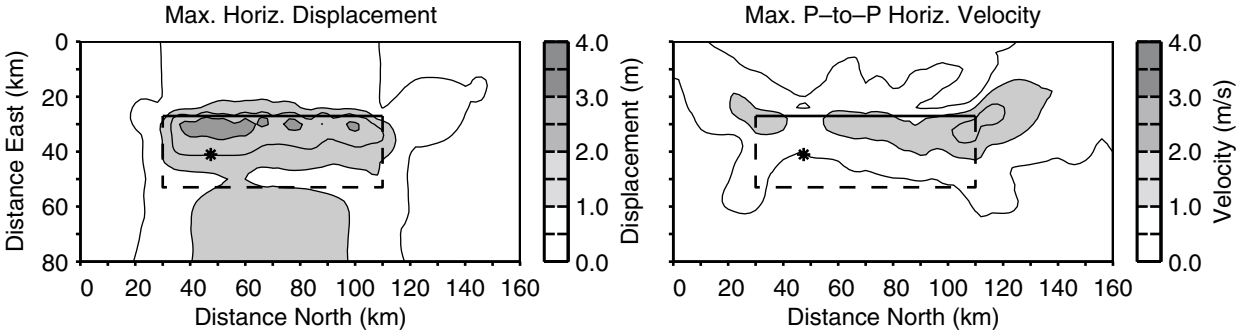

Figure 8. Maximum horizontal displacements and maximum peak-to-peak horizontal velocities on the ground surface for scenario Dip30Rk90HySh (whose geometry is similar to the Chi-Chi earthquake). The thick solid line shows the surface trace of the fault, the thick dashed line indicates the surface projection of the buried edges of the fault, and the asterisk identifies the epicenter. The predominantly mode-III rupture does not efficiently reinforce the Love and Rayleigh waves, which results in much smaller ground motions relative to the other scenarios.

sec at one location, the maximum peak-to-peak velocity is only 1.7 m/sec. On the hanging wall of the fault, the maximum displacements do remain large, although they are dominated by the pseudo-static displacement, which is consistent with equal values of 3.1 m for the maximum amplitude and the maximum peak-to-peak amplitude.

However, moving the hypocenter toward the bottom center of the fault increases the amount of mode-II rupture for the thrust motion cases. Of course, it has the opposite effect for the case of pure strike-slip motion on a vertical fault where the distance over which the portion of the rupture that propagates to the north can effectively reinforce waves decreases by one-third compared with the shallow hypocenter. Thus, for the steeply dipping faults with mostly horizontal slip, the ground motions decrease in most locations when the hypocenter moves to the deeper, more central location, whereas for shallow-dipping faults with a large thrust component of slip, the ground motions increase at many locations. For the 60°-dipping fault with a slip rake angle of 45°, the maximum peak-to-peak velocity is 33% smaller for the deep, central hypocenter compared with the shallow hypocenter. On the other hand, for the 30°-dipping fault with a slip rake angle of 90° (pure thrust), the maximum peak-to-peak velocity increases by 30% when the hypocenter moves from the shallow location to the deep, central location.

Table 2 gives the maximum displacements and the maximum peak-to-peak velocities in the east–west (fault perpendicular), north–south (fault parallel), and vertical directions as well as the maximum in any horizontal direction for each of the 10 scenarios. In all 10 scenarios the ground motions are large, with the maximum displacements exceeding 2.2 m and the maximum peak-to-peak velocities exceeding 1.7 m/sec.

Area Subjected to Levels of Ground Motion

In order to gauge how the severity of shaking changes on a large scale as we transition from pure strike-slip faulting on a vertical fault to thrust faulting on a 30°-dipping fault, we consider three aggregate measures of ground motion: the area on the ground surface where a given level of displacement or velocity is exceeded, how fast the displacements and velocities on the ground surface decay with distance from the fault, and the far-field radiated energy.

Figure 9 gives the areas on the ground surface where the maximum displacements or maximum peak-to-peak velocities exceed a given value for each of the five scenarios with the shallow hypocenter (middepth at the southern quarter point of the fault), where each scenario corresponds to a different dip angle of the fault. In all five cases very large areas (more than 1000 km^2) receive long-period ground motions with displacements or peak-to-peak velocities greater than 1.3 m or 1.0 m/sec. In accordance with the observations noted earlier, the amount of rupture directivity toward the surface controls the amplitude of the motion, so that the largest areas subjected to strong shaking occur in the scenarios with a fault dip angle of 60° or 75°. Moreover, at the strongest levels of shaking, these areas far exceed the corresponding areas for the other scenarios.

The case of pure strike-slip motion on a vertical fault generally falls in the middle ground below the 60°- and 75°-dipping fault scenarios and above the 45°- and 30°-dipping fault scenarios. The curves relating area and maximum displacements for scenarios Dip30Rk90HySh and Dip45Rk22HySh closely follow one another, but the curve relating area and maximum peak-to-peak velocities for scenario Dip45Rk22HySh lies well to the right of the one for scenario Dip30Rk90HySh (similar geometry to the Chi-Chi earthquake). Thus, for the shallow hypocenter the case of pure thrust motion on a 30°-dipping fault results in the smallest area subjected to a given level of peak-to-peak velocity.

Compared with the scenarios with the shallow hypocenter, those with the deep, central hypocenter (5.0 km updip from the bottom center of the fault) exhibit much less variation in the area experiencing a given level of shaking for the various combinations of fault dip and slip rake angles as illustrated in Figure 10. The more central hypocenter near

Table 2

Maximum Displacements and Maximum Peak-to-Peak Velocities in the East–West (Fault-Perpendicular), North–South (Fault-Parallel), Horizontal, and Vertical Directions for Each Scenario

	Max. Disp.				*Max. P-to-P Velocity*			
Scenario	EW (m)	NS (m)	Horiz. (m)	Vert. (m)	EW (m/sec)	NS (m/sec)	Horiz. (m/sec)	Vert. (m/sec)
Dip90Rk0HySh	2.0	2.6	2.6	0.76	2.6	1.0	2.6	0.80
Dip90Rk0HyDp	1.8	2.6	2.6	0.74	2.0	1.1	2.0	0.72
Dip75Rk22HySh	3.1	3.1	3.3	1.4	3.6	1.5	3.7	1.2
Dip75Rk22HyDp	2.1	3.1	3.1	1.3	2.5	1.3	2.8	1.2
Dip60Rk45HySh	3.1	2.8	3.2	2.9	3.9	2.4	4.2	3.0
Dip60Rk45HyDp	2.2	2.8	2.8	2.5	2.4	2.2	2.8	2.2
Dip45Rk68HySh	2.1	2.2	2.2	3.5	2.0	2.5	2.7	3.9
Dip45Rk68HyDp	2.1	2.3	2.3	3.2	1.5	2.4	2.4	2.8
Dip30Rk90HySh (Chi-Chi)	3.1	1.4	3.1	2.5	1.5	1.7	1.7	3.0
Dip30Rk90HyDp	3.1	1.7	3.1	2.8	1.6	2.2	2.2	3.3

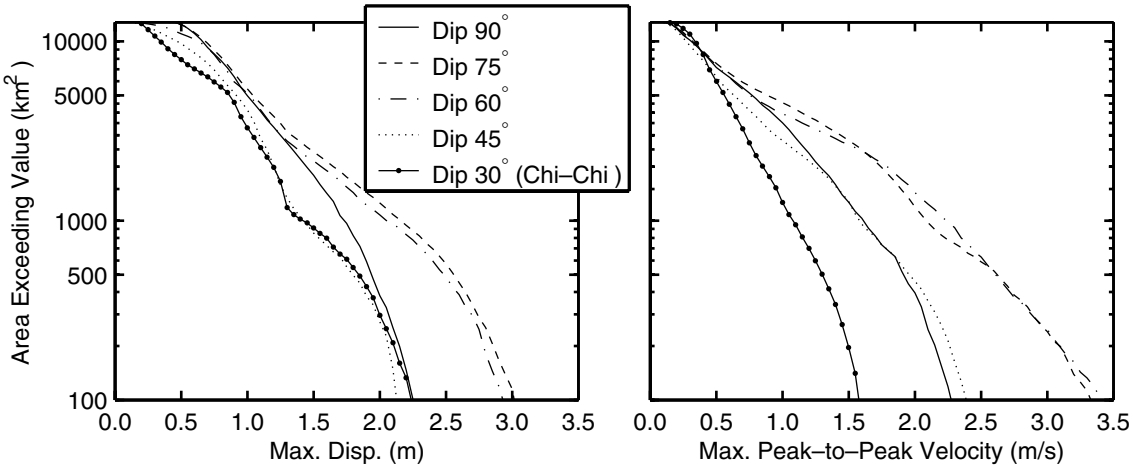

Figure 9. Area on the ground surface where the maximum horizontal displacements (left) and maximum peak-to-peak horizontal velocities (right) exceed a given value for scenarios with the shallow hypocenter. In all five scenarios, areas greater than 1000 km^2 undergo displacements exceeding 1.3 m and peak-to-peak velocities exceeding 1.0 m/sec, with much larger areas for scenarios Dip60Rk45HySh and Dip75Rk22HySh.

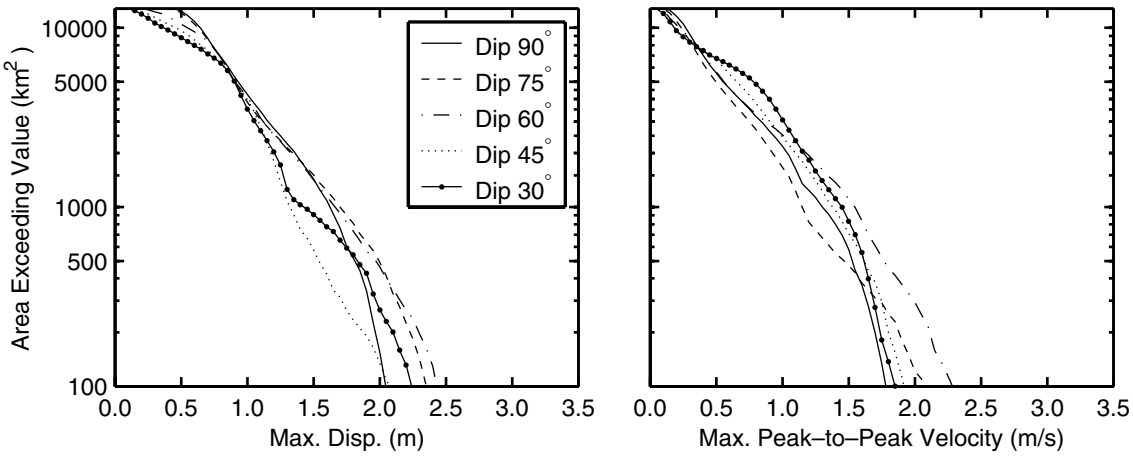

Figure 10. Area on the ground surface where the maximum horizontal displacements (left) and maximum peak-to-peak horizontal velocities (right) exceed a given value for scenarios with the deep, central hypocenter. Shifting the hypocenter to near the bottom center of the fault leads to much smaller variations in the area subjected to a given level of shaking across the five fault dip and slip rake angle pairs.

the bottom of the fault leads to less variation in the distance the rupture propagates in the mode-II direction (direction parallel to slip), because the amount of along-strike rupture decreases while the amount of up-dip rupture increases. This reduces the amount of mode-II rupture in the cases with small slip rake angles, which were dominated by mode-II rupture for the shallow hypocenter, and increases the amount of mode-II rupture in the cases with large slip rake angles, which were dominated by mode-III rupture for the shallow hypocenter. The 60°-dipping fault with a slip rake angle of 45° generally continues to produce the largest areas subjected to a given level of shaking with this different hypocenter, but the curve for pure thrust motion on the 30°-dipping fault shifts toward the middle ground. For some ranges of moderate peak-to-peak velocities, the case of pure thrust motion on the 30°-dipping fault has the largest areas where these levels of motion are exceeded.

Comparing the two scenarios with the 30°-dipping fault, we find that changing the hypocenter has only a small effect on the curve for the maximum displacements, because the slip distribution, which remains the same, largely controls the amplitude of the displacements. On the other hand, moving the hypocenter from the shallow location to the deep, central location shifts the curve for the peak-to-peak velocities toward larger velocities as a result of the increase in the amount of mode-II (in this case up-dip) rupture.

Decay in Ground Motion with Distance

We want to characterize how the ground motions decay with distance from the fault, while also including the effects of rupture directivity and the unpredictability of the hypocenter. We consider identical events occurring along an infinitely long fault and superimpose the distributions of the maximum displacements and velocities for a given scenario such that the ruptures lie end to end, as illustrated in Figure 11. At each location we select the largest values across all of the overlapping domains and then average along the strike of the fault to obtain the average motion on each side of the fault at a given distance. For a discussion of how the displacements and velocities decay with distance from the fault for each scenario as well as comparisons with the Uniform Building Code near-source factor, see Aagaard *et al.* (2002).

In Figure 12 we compare the mean maximum displacements and mean maximum peak-to-peak velocities for scenarios with the shallow hypocenter across the five fault dip angles. On the down-dip (east) side of the fault at distances between 10 and 30 km, the mean values vary remarkably little with the dip angle of the fault. At closer distances and on the up-dip (west) side of the fault, the mean maximum values span a larger range of values; they are lowest for pure thrust motion on the 30°-dipping fault and up to 2 times greater for oblique slip on the 60°- and 75°-dipping faults. These differences arise from the large amount of rupture directivity that occurs for the combination of the shallow hypocenter with the steeply dipping fault geometries and the small amount of rupture directivity that occurs for the same hypocenter with the shallow-dipping fault geometries.

As we found with the area where the maximum motion exceeds a given level, we find less variation in how the mean maximum motion decays with distance from the fault for the deep, central hypocenter (Fig. 13) than for the shallow hypocenter (Fig. 12). Near the trace of the fault, the mean displacements and mean peak-to-peak velocities exhibit only small variations. Likewise, the mean peak-to-peak velocities on the down-dip (east) side of the fault decay in nearly an identical fashion for all five fault dip angles. However, on the up-dip (east) side of the fault, the mean displacements and mean peak-to-peak velocities decay at varying rates for the different fault dip angles. The values decay rapidly for the steeply dipping faults and significantly more slowly for the shallow dipping faults, although the displacements for the 30°-dipping fault drop dramatically from the hanging wall (east side) to the footwall (west side) before decaying slowly with distance.

Radiated Energy

The far-field radiated energy (Fig. 14) displays the same general trends across the 10 scenarios as the velocity amplitudes on the ground surface. We compute the far-field radiated energy by finding the energy dissipated through the damping matrix, which corresponds to the energy in the seismic waves that propagate out to the boundaries of the domain (far field). Consequently, the radiated energy does not account for energy at periods shorter than 2.0 sec, which is not present in our numerical simulations.

The two scenarios with the largest amplitude ground motions (scenarios Dip60Rk45HySh and Dip75Rk22HySh) also radiate the largest amount of energy (1.1×10^{16} J). This is, in large part, due to the greater amount of mode-II rupture in these scenarios. Scenario Dip90Rk0HySh radiates slightly less energy (9.8×10^{15} J). As expected from the amplitude of the ground motions, the smallest radiated energy of 5.5×10^{15} J occurs in scenario Dip30Rk90HySh (Chi-Chi). The slower rupture speed in the mode-III direction relative to the mode-II direction accentuates the relatively smaller amount of radiated energy for the ruptures that are dominated by mode-III rupture. This results from the fact that mode-II propagation is more effective than mode-III propagation in generating far-field shear waves, and these far-field shear waves carry most of the radiated energy.

Moving the hypocenter to the deep, central location results in a 23% increase in the amount of radiated energy for the 30°-dipping fault, while it decreases the radiated energy for the other fault geometries. Note that this increase in the radiated energy stems solely from the shift in the hypocenter and the associated increase in the amount of mode-II rupture. Scenarios Dip75Rk22HyDp, Dip60Rk45HyDp, and Dip45Rk22HyDp all radiate about 7.2×10^{15} J. Consequently, in accordance with the level of long-period shaking, the scenarios with the centrally located deep hypocenter exhibit much less variation in the radiated energy than those with the shallow hypocenter. Overall, we find that the variations in the far-field radiated energy closely follow the trends in the amount of rupture directivity and the relative velocity amplitudes on the ground surface.

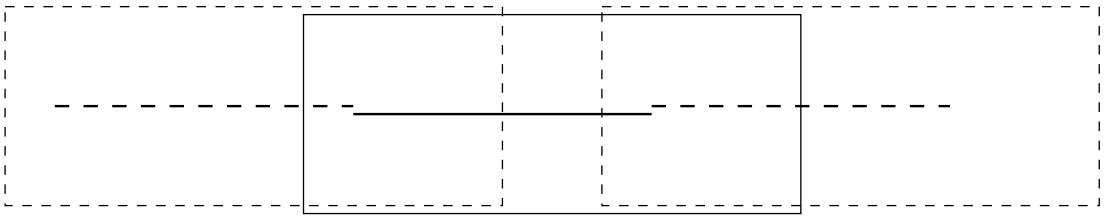

Figure 11. Illustration of how an infinite fault is created from the finite fault in order to examine the decay in ground-motion amplitudes with distance from the fault.

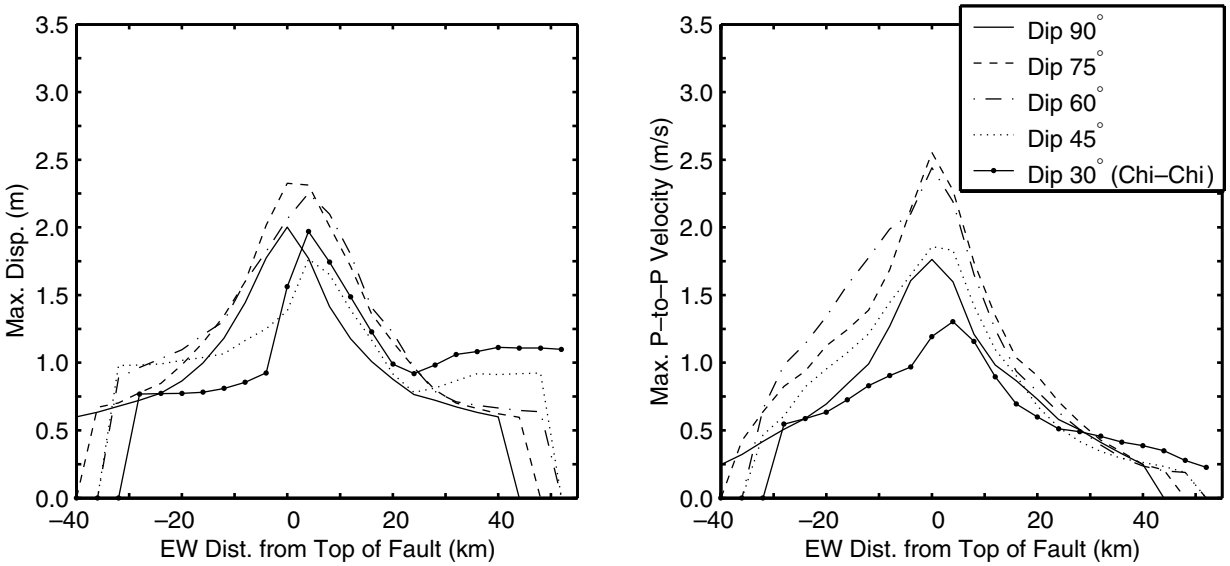

Figure 12. Mean maximum horizontal displacements and mean maximum peak-to-peak horizontal velocities as a function of distance from the fault for scenarios with the shallow hypocenter. Although the mean values do not dramatically differ on the down-dip (east) side of the fault, they span a wide range of values both up-dip (west) of the fault and near the fault trace.

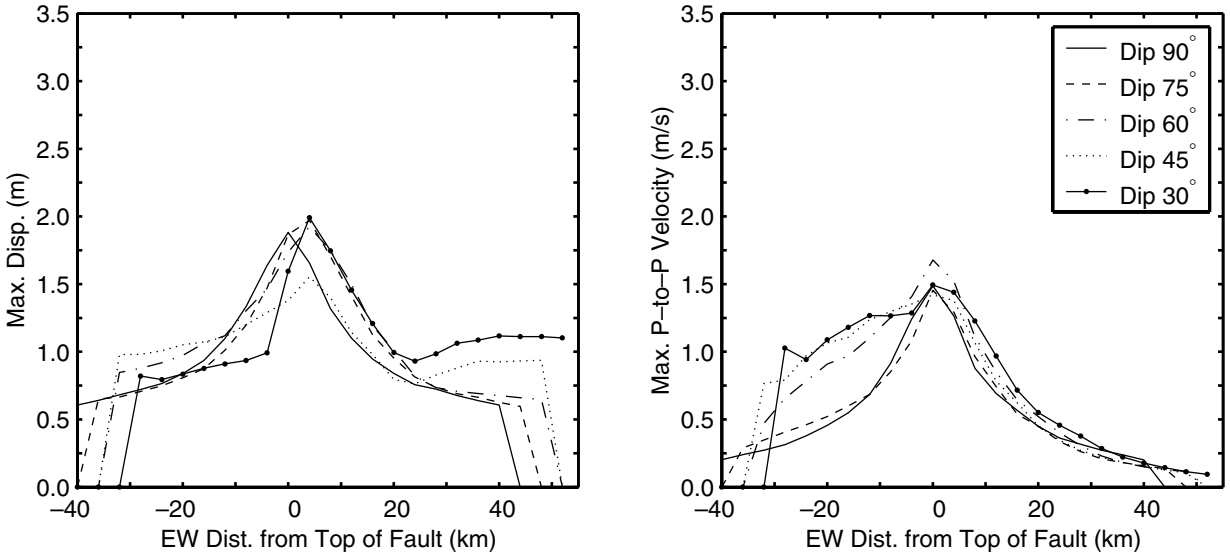

Figure 13. Mean maximum horizontal displacements and mean maximum horizontal peak-to-peak velocities as a function of distance from the fault for scenarios with the deep, central hypocenter. The mean maximum values generally fall within a smaller range for the deep hypocenter compared with the shallow hypocenter. On the up-dip (west) side of the fault, the mean velocities decay more slowly as the fault dip becomes shallower.

Discussion

The 10 scenarios we have discussed illustrate how changes in fault geometry (fault dimensions, fault dip angle, and slip rake angle) determine the amount that a rupture propagates in the mode-II direction, which in turn controls the amount of rupture directivity and the associated area subjected to large-amplitude velocity and displacement pulses. By design, scenario Dip30Rk90HySh approximates the rupture of the Chi-Chi earthquake. Although we do not attempt to model the complex changes in the strike of the fault and the slip rake angle or the physics of the sliding processes, we do match the nominal dip and rake angles (30° and 90°,

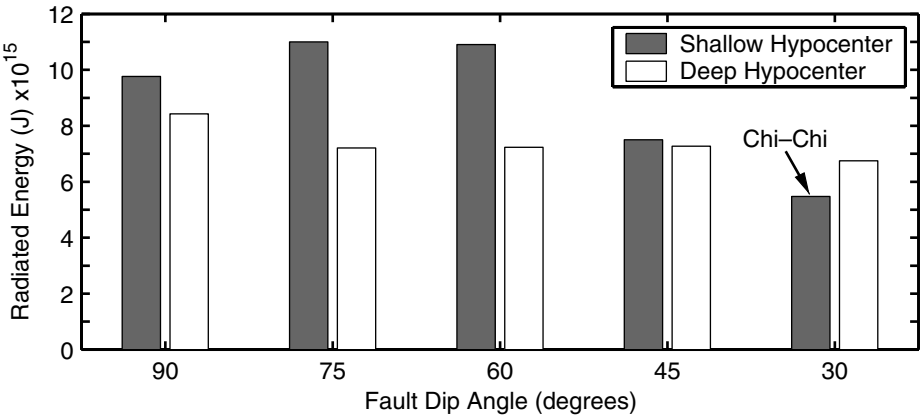

Figure 14. Far-field radiated energy for each of the two hypocenters for each of the five different fault geometries. For predominantly along-strike, unilateral ruptures (shallow hypocenter) the steeply dipping faults radiate considerably more energy than the shallow dipping faults. For predominantly up-dip, bilateral ruptures (deep, central hypocenter) the radiated energies from the five scenarios exhibit much less variation.

respectively), the hypocenter location (approximately 15 km down-dip about one-quarter of the distance along the strike of the rupture), fault area (2400 km^2), and rupture speed (faster in the south where the rupture propagates predominantly up-dip in the mode-II direction and slower in the north where the rupture propagates predominantly along strike in the mode-III direction) (Huang *et al.*, 2000; Ma *et al.*, 2000; Johnson *et al.*, 2001; Ma *et al.*, 2001; Ji *et al.*, 2001). We also do not attempt to match the distribution of slip on the fault but instead use a low-pass filtered random distribution in order to allow creation of the slip distributions for all 10 scenarios using the same procedure. Because we are interested in the rupture directivity, this difference is not as important as matching the geometry.

We compare measured peak horizontal velocities from eight sites surrounding the surface rupture in the near field of the Chi-Chi earthquake with those from six of the simulated scenarios. The sites (locations are shown in Fig. 15) are within approximately 20 km of the surface rupture and include a wide range of azimuths so that we can investigate the distribution of shaking associated with rupture directivity. We avoid sites that lie extremely close to the surface rupture because they are especially sensitive to the amount of nearby slip, which we do not match. We apply the v_0 baseline correction algorithm of Boore (2001) to the Chi-Chi acceleration time histories (Lee *et al.*, 2001) before integrating to obtain velocities. The velocities are low-pass filtered using a third-order Butterworth filter with a corner frequency of 0.5 Hz. The sites for the six simulated scenarios match those of the Chi-Chi stations, and the fault geometry for the 30°-dipping fault approximates the geometry of the Chi-Chi rupture. For the simulated scenarios we align the centers of the surface traces. We also low-pass filter the simulated time histories using a Butterworth filter with the same corner frequency of 0.5 Hz; this has little effect because the seismic source and discretization by design are bandlimited to target periods of 2.0 sec and longer.

The peak horizontal velocities for the 30°-dipping fault and shallow hypocenter (top panel in Fig. 15) indicate that scenario Dip30Rk90HySh matches the limited amount of up-dip rupture directivity that occurred near the epicenter in the Chi-Chi earthquake. The peak velocities in the simulation follow the observed amplitudes reasonably well. The simplifications in the fault geometry along with the uniform rake angles prevent a better match. In the Chi-Chi earthquake, the rotation of the rake angle toward oblique motion in the north increased the amount of rupture directivity (although it remained rather small). As a result, at stations T104 and T120 the peak ground velocities for the Chi-Chi earthquake exceed those from scenario Dip30Rk90HySh, which has a uniform rake angle of 90°.

Given the similarities in the pattern of peak velocities associated with rupture directivity between the Chi-Chi earthquake and scenario Dip30Rk90HySh, one can draw some conclusions about the areas subjected to large-amplitude displacement and velocity pulses for events with geometries that can be approximated by the nine other scenarios. The five other scenarios included in Figure 15 illustrate the basic trends.

Scenarios with strike-slip to oblique motion, such as scenarios Dip60Rk45HySh, Dip60Rk45HyDp, Dip90Rk0HySh, and Dip90Rk0HySh, create significantly more rupture directivity than the Chi-Chi earthquake and scenario Dip30Rk90HySh. In addition to the closer alignment of the slip vector to the predominant direction of rupture propagation in these scenarios, these more steeply dipping faults have a significantly greater rupture length, which also contributes to the increase in rupture directivity and larger-amplitude motions. The ruptures direct most of their energy toward the north or northwest (stations T038 and T104), as

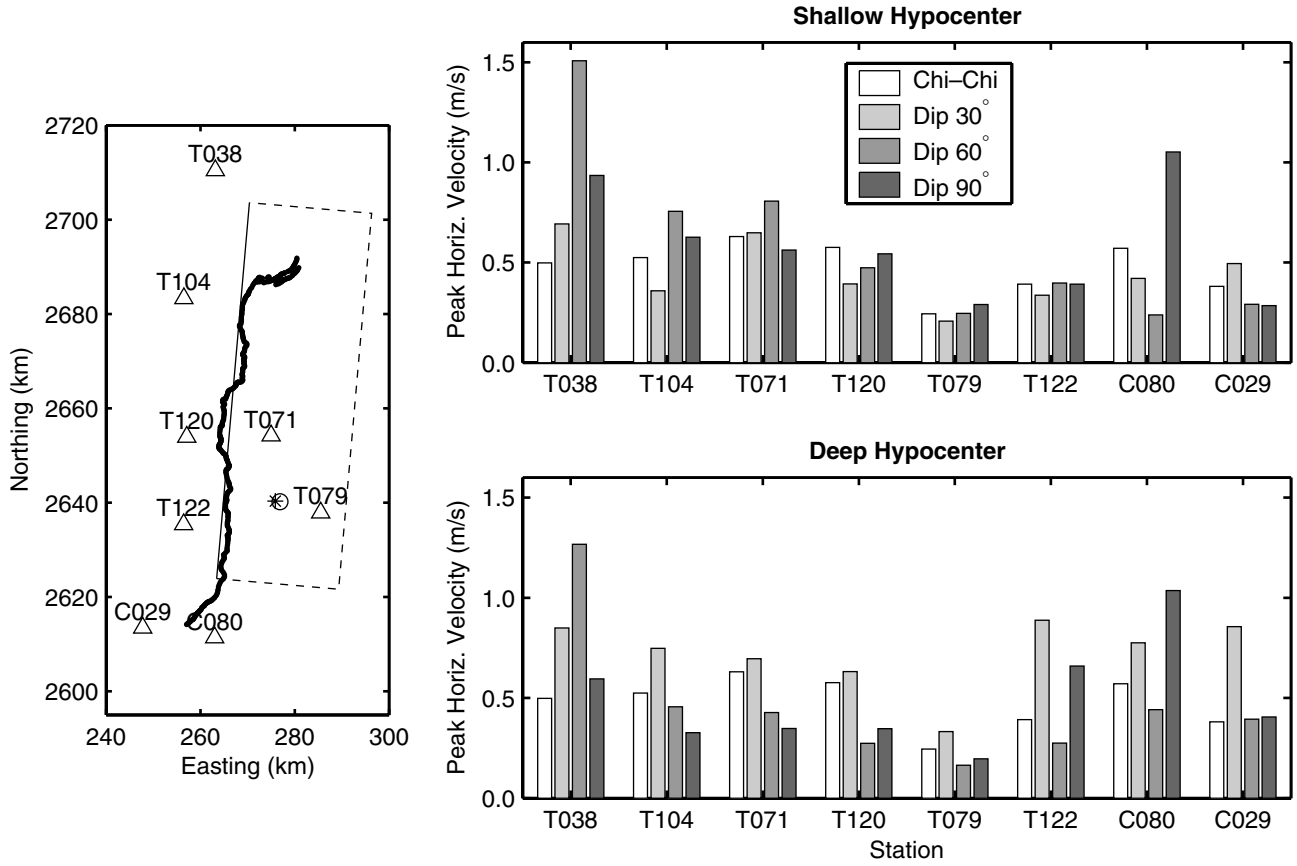

Figure 15. Comparison of peak horizontal velocities across eight stations. The left panel shows the stations (triangles) in the Chi-Chi earthquake used in comparison with the simulations. The thick line shows the surface rupture of the Chi-Chi earthquake, and the asterisk indicates the epicenter. We also overlay the surface projection of the fault (thin and dashed lines) for scenarios Dip30Rk90HySh and Dip30Rk90HyDp with the epicenter for scenario Dip30Rk90HySh indicated by the open circle. The right panel shows the peak horizontal velocities at these eight stations for the Chi-Chi earthquake and simulated scenarios for three fault dip angles for the shallow hypocenter (top) and the deep central hypocenter (bottom). The general agreement between the peak velocities from scenario Dip30Rk90HySh and the Chi-Chi earthquake in the top panel demonstrate that this scenario generates a similar distribution of peak velocities to the Chi-Chi earthquake. Other dip angles and the deep, central hypocenter generate significantly more rupture directivity, which results in larger peak velocities at sites in the forward direction, such as stations T038, T122, and C080.

illustrated by the larger peak velocities in Figure 15, but even sites near the southern end of the fault experience rupture directivity, as demonstrated by station C080 in scenario Dip90Rk0HySh.

The greater rupture directivity increases the area subjected to a given level of shaking as well as the mean maximum velocities as a function of distance from the fault. For example, scenarios Dip60Rk45HySh and Dip90Rk90HySh generate peak-to-peak velocities greater than 1.2 m/sec over areas of 3400 and 2400 km^2, respectively, compared with 700 km^2 for scenario Dip30Rk90HySh (Fig. 9). Similarly, the mean maximum peak-to-peak velocities on the up-dip side of the fault remain above 1.2 m/sec out to distances of only a few kilometers for scenario Dip30Rk90HySh compared with 25 and 10 km for scenarios Dip60Rk45HySh and Dip90Rk0HySh, respectively (Fig. 12). Thus, the Chi-Chi earthquake, with its shallow dip angle and predominantly along-strike rupture, resulted in significantly less rupture directivity and area subjected to large-amplitude velocities compared with other fault geometries with a similar hypocenter.

Returning to Figure 15, scenario Dip30Rk90HyDp (30°-dipping fault with the deep hypocenter) demonstrates how a deeper, more centrally located hypocenter yields more rupture directivity and leads to larger ground motions. The velocities increase at most locations up-dip from the hypocenter, particularly those near the central portion of the fault (stations T104, T120, and T122). Although the greatest mean maximum horizontal displacement is still 2.0 m, the greatest mean maximum peak-to-peak horizontal velocity increases from 1.3 to 1.5 m/sec. Furthermore, the area on the ground surface subjected to a given level of peak-to-peak

velocity increases significantly for peak-to-peak velocities greater than 0.5 m/sec (see Figs. 9 and 10). This suggests that the minimal amount of rupture directivity in the Chi-Chi earthquake confined the large-amplitude motions to locations very close to the fault trace. Hence, the ground motions decayed rapidly with distance from the fault trace. Had the hypocenter been much deeper or more centrally located along the strike of the rupture, we expect that the ground motions would have decayed less rapidly with distance from the fault and been large over a much greater area.

Conclusions

Owing to the presence of shallow slip in the magnitude 7.4 earthquake simulations considered here, Love and/or Rayleigh waves dominate the ground motions; strike-slip faulting tends to generate Love waves, and thrust faulting tends to generate Rayleigh waves. The amount of rupture toward the surface in the direction parallel to slip (mode-II direction and a local maximum in the shear-wave radiation pattern) controls the severity of the long-period shaking. The different levels of long-period motion can be quantified using various measures of the ground shaking, including (1) the area where the displacements and peak-to-peak velocities exceed a given level and (2) the mean maximum displacements and mean maximum peak-to-peak velocities at a given distance from the fault. For strike-slip faulting the shaking is most severe for unilateral rupture, while for thrust faulting the shaking is most severe for up-dip rupture from a deep hypocenter. Figure 16 summarizes how the direction of propagation and the slip rake angle affect the location and degree of rupture directivity. The directivity effect is maximized in the regions where the rupture propagates parallel to the slip vector.

This set of simulations suggests that the amount of rupture directivity in the 1999 Chi-Chi earthquake was small compared to other possible events of the same size that have a deeper, more centrally located hypocenter or have a longer, more steeply dipping fault with oblique motion. Although the complex geometry at the north end of the fault did create some directivity in addition to that which occurred up-dip from the hypocenter, in general, the rupture propagated along a node in the shear-wave radiation pattern, which limited the amount of rupture directivity. As a result, the large-amplitude displacement and velocity pulses that are often associated with near-source ground motions were confined to regions very close to surface rupture or near the surface rupture on the hanging wall. This implies that we should expect severe long-period ground motions over a much larger area when events of the same size occur with other styles of faulting or deeper hypocenters.

Acknowledgments

Access to the Hewlett-Packard V-Class computer, located at the California Institute of Technology, was provided by the Center for Advanced Computing Research. This work was supported in part by the Pacific Earthquake Engineering Research Center through the Earthquake Engineering Research Centers Program of the National Science Foundation under Award Number EEC-9701568. We appreciate the helpful comments from Ned Field, Ken Hudnut, Art McGarr, and two anonymous reviewers.

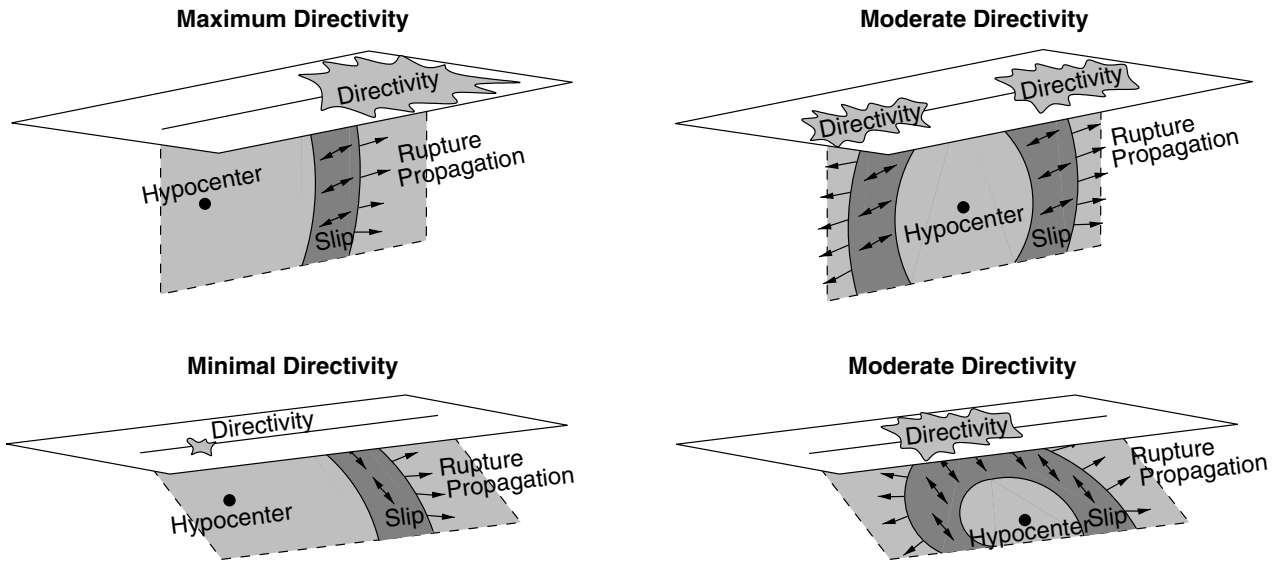

Figure 16. Summary of how the fault geometry and the slip rake angle affect the amount and location of rupture directivity as indicated by the size and location of the splotch on the ground surface. The top row illustrates two cases for a vertical fault with oblique motion, and the bottom row illustrates two cases for a shallow-dipping fault with thrust motion. The left column corresponds to predominantly along-strike rupture (i.e., the shallow hypocenter), whereas the right column corresponds to predominantly bilateral or up-dip rupture (i.e., the deep hypocenter).

References

Aagaard, B. T. (1999). Finite-element simulations of earthquakes, Technical Report 99-03, California Institute of Technology, Earthquake Engineering Research Laboratory, Pasadena, California.

Aagaard, B. T., J. F. Hall, and T. H. Heaton (2001a). Characterization of near-source ground motions with earthquake simulations, *Earthquake Spectra* **17,** no. 2, 177–207.

Aagaard, B. T., T. H. Heaton, and J. F. Hall (2001b). Dynamic earthquake ruptures in the presence of lithostatic normal stresses: implications for friction models and heat production, *Bull. Seism. Soc. Am.* **91,** no. 6, 1765–1796.

Aagaard, B. T., J. F. Hall, and T. H. Heaton (2002). Effects of fault dip and slip rake on near-source ground motions: why the 1999 *M* 7.6 Chi-Chi, Taiwan, earthquake was relatively mild, Technical Report 2002/12, Pacific Earthquake Engineering Research Center, University of California, Berkeley, California.

Allen, C. R., J. R. Brune, L. S. Cluff, and A. G. Barrows (1998). Evidence for unusually strong near-field ground motion on the hanging wall of the San Fernando fault during the 1971 earthquake, *Seism. Res. Lett.* **69,** no. 6, 524–531.

Andrews, D. (1976). Rupture velocity of plane strain shear cracks, *J. Geophys. Res.* **81,** no. 32, 5679–5687.

Archuleta, R. J., and G. A. Frazier (1978). Three-dimensional numerical simulations of dynamic faulting in a half-space, *Bull. Seism. Soc. Am.* **68,** no. 3, 541–572.

Archuleta, R. J., and S. H. Hartzell (1981). Effects of fault finiteness on near-source ground motion, *Bull. Seism. Soc. Am.* **71,** no. 4, 939–957.

Boatwright, J., K. Thywissen, and L. Seekins (2001). Correlation of ground motion and intensity for the 17 January 1994 Northridge, California, earthquake, *Bull. Seism. Soc. Am.* **91,** no. 4, 739–752.

Boore, D. M. (2001). Effect of baseline corrections on displacements and response spectra for several recordings of the 1999 Chi-Chi, Taiwan, earthquake, *Bull. Seism. Soc. Am.* **91,** 1199–1211.

Chen, K.-C., B.-S. Huang, J.-H. Want, W.-G. Huang, T.-M. Change, R.-D. Hwang, H.-C. Chiu, and C.-C. P. Tsai (2001). An observation of rupture pulses of the 20 September 1999 Chi-Chi, Taiwan, earthquake from near-field seismograms, *Bull. Seism. Soc. Am.* **91,** 1247–1254.

Day, S. M. (1982). Three-dimensional simulation of spontaneous rupture: the effect of nonuniform prestress, *Bull. Seism. Soc. Am.* **72,** no. 6, 1881–1902.

Graves, R. W. (1998). Three-dimensional finite-difference modeling of the San Andreas fault: source parameterization and ground-motion levels, *Bull. Seism. Soc. Am.* **88,** no. 4, 881–897.

Hall, J. (1995). Parameter study of the response of moment-resisting steel frame buildings to near-source ground motions, Technical Report 95-08, Earthquake Engineering Research Laboratory, California Institute of Technology, Pasadena, California.

Hall, J. (1997). Response of steel frame buildings to near-source ground motions, Technical Report 97-05, Earthquake Engineering Research Laboratory, California Institute of Technology, Pasadena, California.

Hall, J. F., T. H. Heaton, M. W. Halling, and D. J. Wald (1995). Near-source ground motion and its effects on flexible buildings, *Earthquake Spectra* **11,** no. 4, 569–605.

Haskell, N. (1969). Elastic displacements in the near-field of a propagating fault, *Bull. Seism. Soc. Am.* **59,** no. 2, 865–908.

Heaton, T. H. (1990). Evidence for and implications of self-healing pulses of slip in earthquake rupture, *Phys. Earth Planet. Interiors* **64,** no. 1, 1–20.

Hisada, Y., H. Bao, J. Bielak, O. Ghattas, and D. O'Hallaron (1998). Simulations of long-period ground motions during the 1995 Hyogo-Ken Nanbu (Kobe) earthquake using a 3-D finite element method, in *2nd International Symposium on Effect of Surface Geology on Seismic Motion*, Yokohama, Japan, 1–3 December, 59–66.

Huang, B., K. Chen, W. Huang, J. Wang, T. Chang, R. Hwang, H. Chiu, and C. Tsai (2000). Characteristics of strong ground motion across a thrust fault tip from the September 21, 1999, Chi-Chi, Taiwan earthquake, *Geophys. Res. Lett.* **27,** no. 17, 2729–2732.

Inoue, T., and T. Miyatake (1998). 3-D simulation of near-field strong ground motion based on dynamic modeling, *Bull. Seism. Soc. Am.* **88,** no. 6, 1445–1456.

Iwan, W., and X. Chen (1994). Important near-field ground motion data from the Landers earthquake, in *Proc. of the 10th European Conference on Earthquake Engineering*, Vol. 1, Vienna, 28 August–2 September, 229–234.

Ji, C., D. V. Helmberger, T. Song, K. Ma, and D. J. Wald (2001). Slip history and tectonic implication of the 1999 Chi-Chi earthquake, *Geophys. Res. Lett.* **28,** no. 23, 4379–4382.

Johnson, K., Y. Hsu, P. Segall, and S. Yu (2001). Fault geometry and slip distribution of the 1999 Chi-Chi, Taiwan earthquake imaged from inversion of GPS data, *Geophys. Res. Lett.* **28,** no. 11, 2285–2288.

Kamae, K., and K. Irikura (1998). Source model of the 1995 Hyogo-Ken Nanbu earthquake and simulation of near-source ground motion, *Bull. Seism. Soc. Am.* **88,** no. 2, 400–412.

Lee, W. H. K., T. Shin, W. Kuo, K. Chen, and C. Wu (2001). CWB free-field strong-motion data from the 21 September Chi-Chi, Taiwan, earthquake, *Bull. Seism. Soc. Am.* **91,** 1370–1376.

Ma, K., T. Song, S. Lee, and H. Wu (2000). Spatial slip distribution of the September 20, 1999, Chi-Chi, Taiwan, earthquake (M(w) 7.6): inverted from teleseismic data, *Geophys. Res. Lett.* **27,** no. 20, 3417–3420.

Ma, K., J. Wang, and D. Zhao (1996). Three-dimensional seismic velocity structure if the crust and uppermost mantle beneath Taiwan, *J. Phys. Earth* **44,** no. 2, 85–105.

Ma, K.-F., J. Mori, S.-J. Lee, and S. Yu (2001). Spatial and temporal distribution of slip for the 1999 Chi-Chi, Taiwan, earthquake, *Bull. Seism. Soc. Am.* **91,** no. 5, 1069–1087.

Madariaga, R., K. Olsen, and R. Archuleta (1998). Modeling dynamic rupture in a 3-D earthquake fault model, *Bull. Seis. Soc. Am.* **88,** no. 5, 1182–1197.

Mai, P., and G. Beroza (2002). A spatial random-field model to characterize complexity in earthquake slip, *J. Geophys. Res. Solid Earth* **107,** no. B11, 2308, doi 0.1029/2001JB000588.

Nielsen, S., and K. Olsen (2000). Constraints on stress and friction from dynamic rupture models of the 1994 Northridge, California, earthquake, Pure Appl. Geophys. **157,** no. 11–12, 2029–2046.

Oglesby, D. D., and S. M. Day (2001). Fault geometry and dynamics of the 1999 Chi-Chi (Taiwan) earthquake, *Bull. Seism. Soc. Am.* **91,** 1099–1111.

Oglesby, D. D., R. J. Archuleta, and S. B. Nielsen (2000). The three-dimensional dynamics of dipping faults, *Bull. Seism. Soc. Am.* **90,** no. 3, 616–628.

Olsen, K., and R. Archuleta (1996). Three-dimensional simulation of earthquakes on the Los Angeles fault system, *Bull. Seism. Soc. Am.* **86,** no. 3, 575–596.

Olsen, K., R. Madariaga, and R. Archuleta (1997). Three-dimensional dynamic simulation of the 1992 Landers earthquake, *Science* **278,** 834–839.

Olsen, K. B., R. J. Archuleta, and J. R. Matarese (1995). Three-dimensional simulation of a magnitude-7.75 earthquake on the San-Andreas Fault, *Science* **270,** no. 5242, 1628–1632.

Ouchi, T., A. Lin, A. Chen, and T. Maruyama (2001). The 1999 Chi-Chi (Taiwan) earthquake: earthquake fault and strong motions, *Bull. Seism. Soc. Am.* **91,** 966–976.

Pitarka, A., K. Irikura, T. Iwata, and S. Sekiguchi (1998). Three-dimensional simulation of the near-fault ground motion for the 1995 Hyogo-ken Nanbu (Kobe), Japan, earthquake, *Bull. Seism. Soc. Am.* **88,** no. 2, 428–440.

Somerville, P. G., N. F. Smith, R. W. Graves, and N. A. Abrahamson (1997). Modification of empirical strong ground motion attenuation relations to include the amplitude and duration effects of rupture directivity, *Seism. Res. Lett.* **68,** no. 1, 199–222.

Wald, D. J., V. Quitoriano, T. H. Heaton, and H. Kanamori (1999). Rela-

tionships between peak ground acceleration, peak ground velocity, and modified Mercalli intensity in California, *Earthquake Spectra* **15,** no. 3, 557–564.

Wells, D., and K. Coppersmith (1994). New empirical relationships among magnitude, rupture length, rupture width, rupture area, and surface displacement, *Bull. Seism. Soc. Am.* **84,** no. 4, 974–1002.

U.S. Geological Survey
525 South Wilson Ave.
Pasadena, California 91106
(B.T.A.)

Department of Civil Engineering
Mail Stop 104-44
California Institute of Technology
Pasadena, California 91125
(J.F.H.)

Department of Geologic and Planetary Sciences
Mail Stop 252-21
California Institute of Technology
Pasadena, California 91125
(T.H.H.)

Manuscript received 17 March 2003.